Yuanchong Zhang [1,2], and William B. Rossow[3]

[1] SciSpace LLC, 2880 Broadway, New York, NY 10025, USA.

[2] NASA Goddard Institute for Space Studies, 2880 Broadway, New York, NY 10025, USA.

[3] Franklin, New York.

Corresponding author: Yuanchong Zhang (yz7@columbia.edu)

Key Points:

- The radiative flux profile data product (called ISCCP-FH) is described. It benefits from the new ISCCP cloud products (called ISCCP-H).
- The product is evaluated against the Clouds and the Earth's Radiant Energy System and the Baseline Surface Radiation Network measurements.
- The long-term variations of TOA, surface and in-atmosphere net fluxes are documented and the possible cloud feedback is investigated.

Abstract

The third generation of the radiative flux profile data product, called ISCCP-FH, is described. The revisions over the previous generation (called ISCCP-FD) include improvements in the radiative model representation of gaseous and aerosol effects, as well as a refined statistical model of cloud vertical layer variations with cloud types, and increased spatial resolution to 110 km. The new product benefits from the changes in the new H-version of the ISCCP cloud products (called ISCCP-H): higher spatial resolution, revised radiance calibration and treatment of ice clouds, treatment of aerosol effects, and revision of all the ancillary atmosphere and surface property products. The ISCCP-FH product is evaluated against more direct measurements from the Clouds and the Earth's Radiant Energy System and the Baseline Surface Radiation Network products, showing some small, overall reductions in average flux uncertainties; but the main results are similar to ISCCP-FD: the ISCCP-FH uncertainties remain 10 Wm^{-2} at the top-of-atmosphere (TOA) and 20 Wm^{-2} at surface for monthly, regional averages. The long-term variations of TOA, surface and in-atmosphere net fluxes are documented and the possible transient cloud feedback implications of a long-term decline of clouds are investigated. The cloud and flux variations from 1998 to 2012 suggest a positive cloud-radiative feedback on the oceanic circulation and a negative feedback on the atmospheric circulation. This example demonstrates that the ISCCP-FH product can provide useful diagnostic information about weather-to-interannual scale variations of radiation induced by changes in cloudiness as well as atmospheric and surface properties.

Plain Language Summary

(optional)

1 Introduction

Earth's climate is determined by a long-term, global balance of energy exchanges in the form of radiative fluxes, water phase changes, surface-atmosphere exchanges, and transports by the oceanic and atmospheric circulations; but the circulations and their transports are modified by the short-term, local imbalances of the energy and water exchanges. The atmospheric circulations (weather) produce water phase changes in the form of clouds and precipitation that feedback on all of these exchanges and circulation transports. The early focus of weather studies was on the precipitation produced from clouds. The early focus of climate studies was on the modulation of the top-of-atmosphere (TOA) radiative fluxes by cloud variations, usually the global average changes that are associated with global mean surface temperature changes. However the global mean temperature is not simply related to the average energy balance because changes in the atmospheric and oceanic circulation redistribute the energy, complicated by induced cloud feedbacks on these circulations. Hence, fully diagnosing cloud-radiative feedbacks on weather and climate requires decomposing the space-time variations of TOA fluxes into surface (SRF) fluxes that affect the ocean circulation and atmospheric (ATM) flux profiles that affect the atmospheric motions and cloud (precipitation) formation. Since the solar (shortwave, SW) fluxes act primarily on the surface and the terrestrial (longwave, LW) fluxes act primarily on the atmosphere, these have to be diagnosed separately. This diagnosis has to be done across a range of space-time scales to establish the coupling at different scales of atmosphere-ocean motions.

Obtaining global observations that directly resolve bulk-cloud-process-scale variation of surface fluxes and atmospheric profiles of radiation is infeasible, so another approach is to measure the space-time-resolved variations of the properties of the clouds, atmosphere and the surface and then calculate the radiative fluxes with a detailed radiative transfer model. Atmospheric radiative transfer is sufficiently advanced that the accuracy of such calculations is primarily limited by the accuracy and completeness of the description of the cloud, atmosphere and surface properties input to the model. The knowledge and accuracy of this information has increased over the past few decades so that such calculations can improve to reliably reveal more detailed radiative exchanges and their variations.

This paper summarizes continuing work along these lines by describing a new data product, called ISCCP-FH, providing radiative flux profiles at 110 km, 3-hr intervals, covering the whole globe for 35 years (Zhang, 2017). This product is a revision of previous versions based on earlier ISCCP data products (Zhang et al., 1995, 2004). The new flux profiles are based on the new ISCCP-H cloud and atmosphere products (Young et al., 2018; Rossow et al., 2022) using a revised radiative transfer model with a refined statistical model of cloud vertical structure. The decadal-scale changes to the radiative transfer model and the input data are described in Sections 2 and 3, respectively. The resulting products are described and evaluated compared with more direct measurements of surface and top-of-atmosphere fluxes in Section 4. Some basic results and the long-term variations in the fluxes, especially the partitioning of the TOA fluxes

into SRF and ATM net fluxes and their average latitude variations, are summarized in Section 5. Section 6 discusses some possible implications for feedbacks on atmosphere-ocean circulations of one example of changes in the net flux distributions. In conclusion Section 7 suggests other diagnostic studies that can be done with this data product.

2 Changes in the radiative model

Revisions of the radiative transfer model for calculating the flux profiles from the previous version (see Zhang et al., 2004 for details) are: (1) reformulation of the SW line absorption for H2O, O2, CO2, CH4, N2O, etc., using the latest HITRAN2012 atlas (Rothman et al., 2013) with added weak-SW-absorption values for H2O, O2 and CO2, (2) improved LW modeling of the H2O continuum, CFC absorption cross-sections, SO2 line absorption, and CH4 and N2O overlap, especially in polar conditions, (3) refined LW treatment for large water vapor amounts (e.g., DeAngelis et al., 2015), including accounting for within-layer water vapor gradients, and (4) increased base number of vertical layers from 24 to 43 for LW flux calculation. The code has an estimated accuracy of 1 Wm^{-2} for net LW fluxes throughout the troposphere and most of the stratosphere and close to 1% for SW fluxes as compared with line-by-line calculations (cf. Lacis and Oinas, 1991). This code is equivalent to the current radiation code of ModelE2.1 of the NASA Goddard Institute for Space Studies (GISS) (Kelley et al., 2020). In applying it for ISCCP-FH production, the monthly-mean aerosol data in the model is replaced by the MAC-v2 global dataset over all years (Kinne, 2019) for better treatment of the spectral details of stratospheric and tropospheric aerosol scattering and absorption. Daily total solar irradiance (TSI) is changed to the Solar Radiation and Climate Experiment (SORCE, V-15) based dataset, which is equivalent to that used in the CERES products. Other changes of input parameters are based on the ISCCP-H data product. The FH horizontal resolution is increased to 1° equal-area for consistency with the ISCCP-H data product (see next section).

3 Changes in input datasets

Notable changes to produce ISCCP-H (Rossow, 2017; Young et al., 2018; Rossow et al., 2022), now covering 1983-2018, are: (1) refinements of cloud microphysical models (effective particle sizes for liquid clouds changed to 13 m over land and 15 m over ocean and for ice clouds changed to 20 m for clouds with optical thickness (TAU) < 3.6 and 34 m for thicker clouds), (2) introduction of finite cloud layer thicknesses in the retrieval that vary from 100 to 200 hPa from the surface to the tropopause, (3) change of the ratio of ice and liquid cloud amounts from 0.96 to 0.64 by lowering the threshold temperature from 260 K to 253 K, (4) a reduction of cloud amount (CA) over high topography ice sheets in summer by about 0.10 (the only significant change), (5) placement of very thin cirrus at the tropopause instead above it, (6) treatment of stratospheric and tropospheric aerosol radiative effects in the cloud and surface retrievals, (7) treatment of surface temperature inversions and retrieval of physical surface temperatures (with correction of extreme values), and (8) 1° equal-area mapping

of satellite pixels sampled at 10 km intervals.

All new ancillary inputs for FH (land-water mask, topography, sea ice and snow cover, total ozone abundance, stratospheric and tropospheric aerosol properties, atmospheric profiles of temperature and relative humidity) come from ISCCP-H (Young et al., 2018). These datasets have higher space-time resolutions and are more homogeneous over their records. In particular, the atmospheric dataset provides global 3-hr temperature-relative humidity profiles at 16 atmospheric levels with surface temperature inversions.

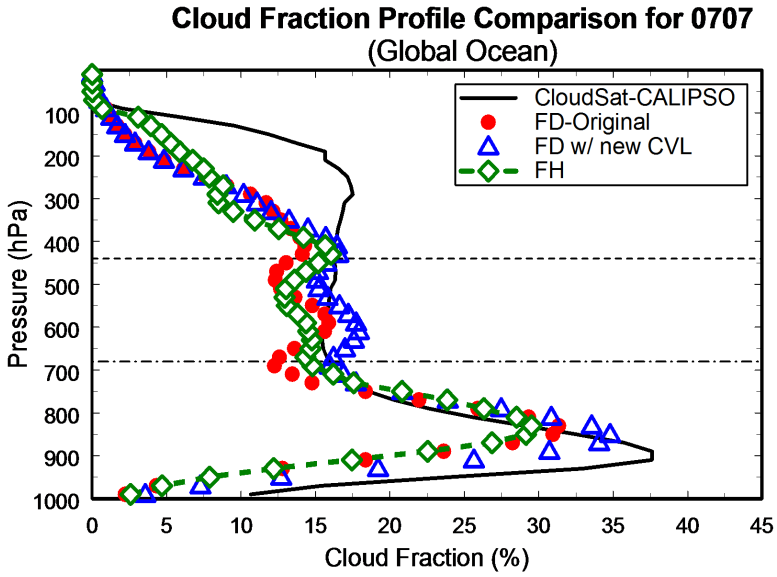
Cloud Fraction Profile Comparison for 0707
(Global Ocean)
CloudSat-CALIPSO
FD-Original
FD w/ new CVL
FH
Pressure (hPa)
100
200
300
400
500
600
700
800
900
1000
0
5
10
15
20
25
30
35
40
45
Cloud Fraction (%)

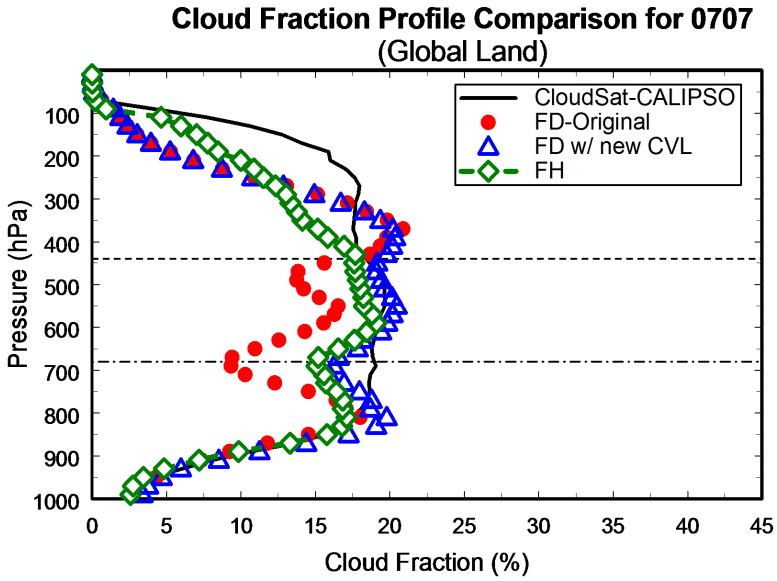
Cloud Fraction Profile Comparison for 0707
(Global Land)
CloudSat-CALIPSO
FD-Original
FD w/ new CVL
FH
Pressure (hPa)
100
200
300
400
500
600
700
800
900
1000
0
5
10
15
20
25
30
35
40
45
Cloud Fraction (%)

Figure 1. Average cloud amount (%) at each pressure (hPa) for July 2007 over ocean (upper panel) and land (lower panel) from CloudSat-CALIPSO (solid black line), the original profile used for ISCCP-FD (red dots), the profile produced by the new cloud vertical layer model (CVL) applied to ISCCP-D cloudiness (blue triangles), and applied to ISCCP-H cloudiness (green diamonds) as used in ISCCP-FH. The horizontal dashed black lines indicate the pressure boundaries separating low, middle and high cloud tops.

The cloud vertical layer (CVL) model has been revised based on comparison of the earlier version (Rossow et al., 2005) with CloudSat-CALIPSO cloud profiles (Rossow and Zhang, 2010). The new statistical model used in FH is shown in Fig. 1 compared with the older model and with CloudSat-CALIPSO RL-GeoProf (P2_R04 − this is the 1/3 km lidar version). This version of GeoProf uses Version 3 of the CALIPSO products that made significant changes in the amount of low cloud relative to the earlier version (Mace and Zhang, 2014); however Version 4 of CALIPSO makes more changes, including in the amount of upper troposphere cloud (Liu et al., 2019). Also shown is the new model applied to ISCCP-D clouds. Although the FH CVL model makes adjustments of the ISCCP cloud distribution (see Zhang et al., 2004) to increase low cloud amount to account for higher-layer-obscuration and to increase thin high-level cloud amount to account for misplacement of some of these clouds to lower levels, the results still underestimate low-level cloud amount over oceans by about 0.05 and cloud amount at the highest levels in general by about 0.05-0.10. The continued refinement of the CloudSat and CALIPSO products makes the magnitude of these underestimates uncertain. (At the time of writing, the "active release versions for 2B-GEOPROF-LIDAR are R04 & R05; P1_R05 is the current version and R04 products will be available until all R05 products have been released," see https://www.cloudsat.cira.colostate.edu/data-products/2b-geoprof-lidar).

Gas abundances (except for water vapor and ozone) are specified as in the GISS climate model, including positive trends in CO2 and CH4 abundances from observations (e.g., Hansen et al., 1988; the most up-to-date trends can be found in "Forcings in GISS Climate Model" at https://data.giss.nasa.gov/modelforce/ghgases/). Surface albedos (except for water) are derived from an aerosol-corrected surface visible reflectance and a spectral dependence model (6 bands) for different surface types (although the surface reflectance in ISCCP-H in the visible have been corrected for stratospheric and tropospheric aerosol scattering/absorption using MAC-v1, Kinne et al., 2013, the adjustment in FH is done using the full spectral dependence of a later version of the aerosol product, MAC-v2, Kinne et al., 2019). Surface temperatures from ISCCP-H are physical values obtained using estimated narrowband emissivities (at ~11 m wavelength) by surface type (Rossow, 2017); broadband emissivities by surface type are used in FH calculations (Zhang et al., 2007). The diurnal variations of surface air and skin temperatures from ISCCP-H (which are clear-sky biased) are corrected for cloud effects (Zhang et al., 2006).

4 Product description and evaluation

The FH products report the upward and downward SW and LW fluxes at five levels from the surface to the top-of-atmosphere for "full" sky (actual variable cloud cover), clear sky and overcast sky, as well as the diffuse and direct SW fluxes at the surface. These results are compiled in five sub-products (all in NetCDF except the last): FH-TOA (radiative fluxes at top of atmosphere with relevant physical quantities, 23 variables), FH-SRF (radiative fluxes at surface with relevant physical quantities, 34 variables), FH-PRF (flux profiles at the surface, 680 hPa, 440 hPa, 100 hPa, top-of-atmosphere at about 100 km altitude, 91 variables), FH-MPF (monthly average of FH-PRF) and FH-INP (complete inputs up to 355 variables). All of these products are mapped at 1^{o}-equivalent-equal-area and all, except MPF, are reported at 3-hr intervals.

Extensive comparisons of the previous versions of this product set the stage for documenting the small changes/improvements made in the ISCCP-FH product (Zhang et al., 1995; Rossow and Zhang, 1995; Zhang et al., 2004, 2006, 2007, as well as Raschke et al., 2016). Zhang et al. (1995) conducted a complete set of sensitivity studies to determine how uncertainties in the inputs translate to flux uncertainties (still valid for FH), emphasizing the leading importance of clouds for SW fluxes and atmospheric and surface temperatures for LW fluxes. They highlighted the dominance on small space-time scales of sampling differences in comparisons of the calculated fluxes with direct measurements, but also showed that differences in monthly averages better indicated biases in inputs to the calculations. Rossow and Zhang (1995) conducted a detailed set of comparisons with direct TOA and SRF flux measurements, investigating in particular the effects of differences in space-time sampling and coverage in such comparisons. The mismatch of spatial scales exaggerates the differences for surface flux comparisons by 30-100% because the meteorological conditions do not always match (Rossow and Zhang, 1995; Zhang et al., 2010). The better matching of satellite products contributes less uncertainty. More detailed evaluations of the input quantities, other than clouds, were conducted in Zhang et al. (2006, 2007) and more general evaluations of the previous flux products were made in Rossow and Zhang (1995) and Zhang et al. (2004).

Table 1. Comparison of 2007 monthly mean ISCCP-FH and FD TOA fluxes with CERES (Edition 3A, CERES Science Team, 2013) and SRF fluxes with BSRN (Ohmura et al., 1998) in Wm^{-2}. The uncertainty range is based on the normal deviations (rms distance of each point from the least squares linear fit) (Rossow and Zhang, 1995).

TOA		
	FH vs CERES	FD vs CERES
SWnet	-7 ± 6	-8 ± 6
Correlation for SWnet	0.99	0.99
LWnet	+7 ± 3	+3 ± 3
Correlation for LWnet	0.99	0.99

TOA		
Overall uncertainty	10 Wm^{-2}	10 Wm^{-2}
Surface		
	FH vs BSRN	FD vs BSRN
SWnet	-1 ± 15	-4 ± 17
Correlation for SWnet	0.99	0.99
LWnet	-7 ± 12	+10 ± 14
Correlation for LWnet	0.97	0.97
Overall uncertainty	20 Wm^{-2}	20 Wm^{-2}

A summary estimate of the uncertainties of FH and FD fluxes is shown in Table 1 based on monthly mean comparisons for 2007 at 1° mapping to CERES (SYN1deg Ed3A, see CERES Science Team, 2013) for TOA fluxes and collocated Baseline Surface Radiation Network stations (BSRN, Ohmura et al., 1998; Driemel et al., 2018) for SRF fluxes. Comparisons were also made by Stackhouse et al. (2021) to the latest version of GEWEX-SRB Rel4 (which is also based on ISCCP-H) with respect to CERES Energy Balanced and Filled (EBAF) Ed4.1 (Loeb et al., 2018), which is an adjusted version of Ed3A to reduce the original net imbalance of +4.3 Wm^{-2} to force agreement with an imbalance estimate of < 1 Wm^{-2} from ocean heat measurements. The results from Stackhouse et al. (2021) do not change the comparison statistics for the overall biases (and standard deviation). Table 2 shows the evolution of such comparison differences for the three versions of these products (including alternate versions of the CERES products, cf. Stackhouse et al., 2021).

Table 2. Evolution of flux biases (Wm^{-2}) from comparisons with spatially matched ERBE or CERES at top-of-atmosphere and GEBA (Wild *et al.* 2017) or BSRN at surface (Driemel *et al.* 2018)†.

TOA			
	FC – ERBE	FD – ERBE	FH – CERES
SWup	+10.7	+4.7	+7.2 (+7.5, +5.0)
LWup	−1.1	−2.2	−7.1 (−7.0, −8.0)
Net	−9.3	−2.0	0.0 (−0.5, −3.2)
Surface			
	FC – GEBA	FD – BSRN	FH – BSRN
SWdn	+15.2	+2.0	−1.4
LWdn	−19.4	+2.2	−7.5
Net	N/A	N/A	(+4.1)

†The FC comparisons are based on 16 seasonal months over 1985 – 1989 as reported in Rossow et al. (1995). The FD comparison with ERBE is also based on the same 16 seasonal months as FC but the FD comparison with BSRN is based

on all months over 1992 – 2001 as reported in Zhang et al. (2004). The FH comparisons are based on monthly means in 2007 from CERES (SYN1deg Ed3a) and BSRN; values in parentheses represent the bias with respect to CERES SYN1deg 4.1 for 2007–2009 period and EBAF 4.1 and 2001–2009 period, respectively, cited from Stackhouse et al. (2021).

The comparison statistics (more details not shown) indicate that the FH results are only a very slight improvement over the FD results (Zhang et al., 2004). Clear sky SW absorption has increased producing better agreement with line-by-line calculations (cf. Oreopoulos et al., 2012). As noted below some changes in surface LW fluxes are associated with the change of atmospheric temperature-humidity inputs. The detailed changes in cloud microphysics did not produce notable changes in the fluxes overall.

The dominant source of uncertainty in the flux profiles is still associated with the cloud vertical structure model, which is a small improvement over the previous version (Fig. 1). The new model still underestimates cloud amounts near the tropopause (at the 200 hPa level) by about 0.05 (land) and 0.10 (ocean). Based on the GEWEX assessment of ISCCP-D clouds (Stubenrauch et al., 2013), some of these high clouds (about 0.05) are actually missed by ISCCP-D, but they have such low optical thicknesses that the resulting flux biases are estimated to be $<$ 1 Wm^{-2} (Zhang et al., 2004). Most of the near-tropopause clouds are actually detected but displaced to lower levels; as shown by Chen and Rossow (2002), even though these clouds are consistent with the narrowband IR radiances, they are below the water vapor emission level at wavelengths $>$ 25 m, which may account for part of an underestimate of LW emission (LWup) at TOA. The new cloud vertical model also underestimates low-level cloud amount by about 0.05 and top pressure by about 75 hPa over oceans, which may produce an underestimate of downward LW (LWdn) at the ocean surface. Although Fig. 1 does not show similar underestimates of low cloud amount over land relative to GeoProf, the BSRN comparison still indicates a small low bias of LWdn at the surface in FH, which may indicate an underestimate of low clouds over land as well. However, the larger effect on LWdn at the surface is associated with the change in atmospheric temperature-humidity profiles: the new product in ISCCP-H (called NNHIRS) has near-surface air temperatures within 1-2 K over land compared to surface measurements but is drier at the surface over land (where the BSRN stations are) (Rossow et al., 2022).

The bias of FH upwelling SW (SWup) flux at TOA with respect to CERES is consistent in sign with the bias of downwelling SW (SWdn) flux at SRF with respect to BSRN, an improvement over the FC/FD SW biases that were not consistent at TOA and SRF (Table 2). The bias of SWdn and LWdn at SRF is much smaller for FD and FH compared to BSRN than for FC compared to GEBA. The smaller bias of LWup at TOA in FC/FD when compared with ERBE becomes larger for FH when compared to CERES, even though the latter is smaller than ERBE and FH is smaller than FC/FD. These differences for FH are still within the uncertainties of the comparison datasets as discussed next.

The datasets used for evaluation of FC/FD/FH have their own uncertainties, including uncertainty in calibration; the latter is smaller for CERES/BSRN than for ERBE/GEBA. Thus, some of the changes (especially biases) in the comparison results could be caused by changed reference data (Table 2). In addition, there are differences in the wavelength ranges defining SW and LW fluxes (measurements are corrected for limited instrument sensitivity), treatment of angle dependence (measurements are corrected) and domain area represented (smaller for surface measurements than satellite-based products).

ERBE/CERES separate SW and LW at 5.0 m, calibrating to account for instrument sensitivity ranges that do not correspond precisely to this division. The ERBE scanners were sensitive in the (approximate) wavelength range of 0.2 to 4.5 m in the SW and 6 to 35 m in the LW; the ERBE LW is truncated at 50 m (Barkstrom et al., 1989). The CERES instruments are sensitive in the range 0.3 to 5 m in the SW and 5 to 200 m in the LW (Loeb et al., 2018), which is determined from a Total channel (0.3 to 200 m) with a decreasing sensitivity longward of 30 m (Loeb et al., 2001). For surface SW instruments, corrections are needed for the dome transmission (estimated at about 0.95) and an uncertain thermal offset; LW instruments have various shortwave cutoffs at 3.5-5.0 m to exclude sunlight, but there is some thermal radiation in this wavelength range (Kohsiek et al., 2006). Philipona et al. (2001) describe the typical wavelength coverage by SW instruments as 0.3-2.8 m and LW as 4.0-50 m, with as much as 2% of the LW flux at wavelengths > 50 m; they estimate the resultant flux uncertainties of SW ± 5 Wm^{-2} and LW ± 10 Wm^{-2}. FH (as well as FC/FD) includes wavelengths 0.2-15.0 m in the SW radiation from the sun, but without thermal radiation from Earth, and includes wavelengths 0.2-200 m in the LW radiation from Earth (for a complete Planck function), but without solar radiation. Effectively, however, the calculated fluxes represent 0.2-5.0 m for SW and 5.0-200 m for LW.

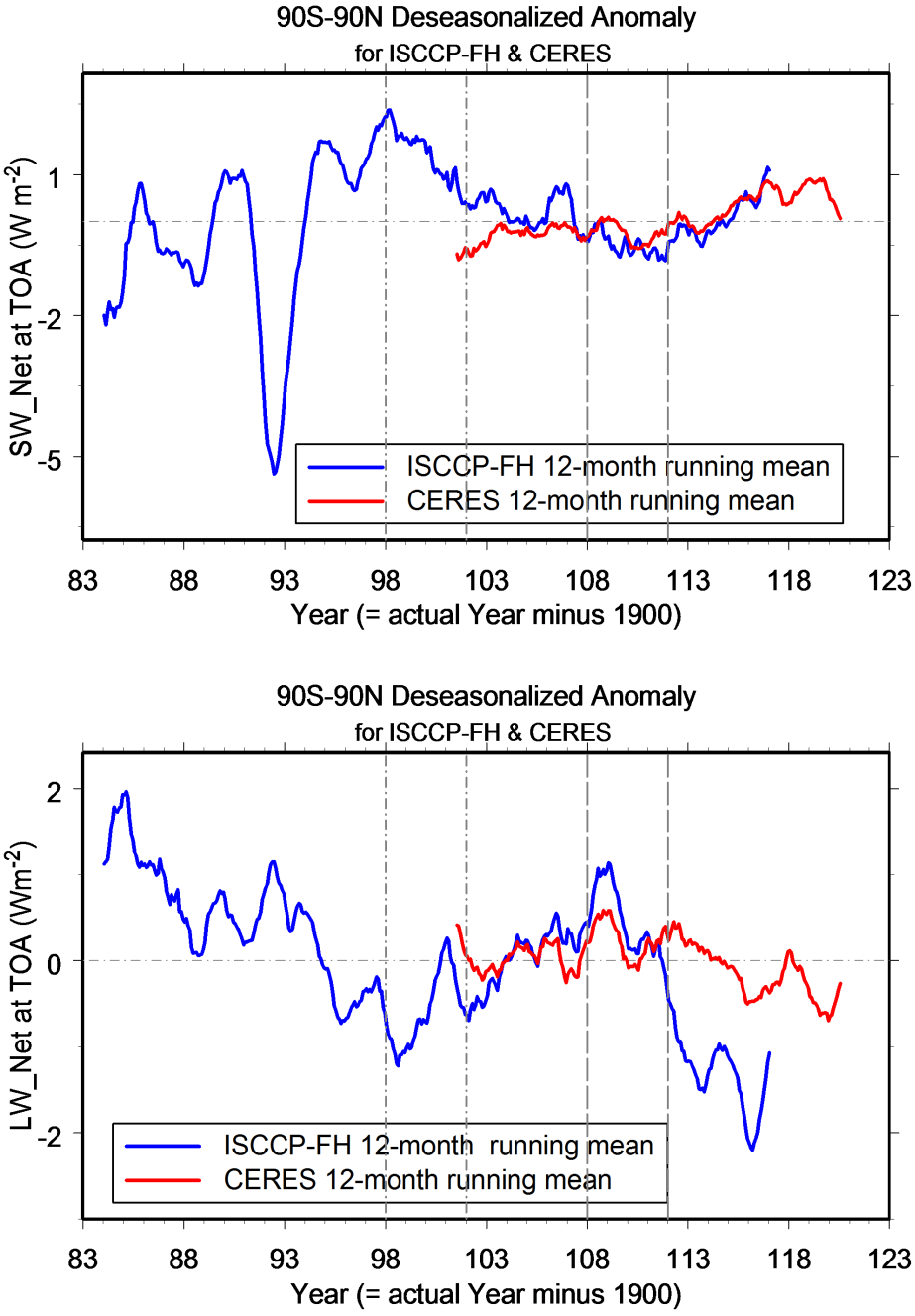

Figure 2. Deseasonalized anomalies (shown as 12-month running averages) of

global monthly mean TOA net fluxes (Wm^{-2}) from FH (blue curves) compared to CERES (SYN1deg Ed4.1, red curves) for SWnet (upper panel) and LWnet (lower panel) from 1983 to 2019, where FH covers July 1983 to June 2017 while CERES covers 2001 to 2020. The anomalies for each dataset are determined relative to their own record averages. Positive SWnet anomaly indicates more absorption (lower planetary albedo) and positive LWnet anomaly indicates decreased emission. The vertical lines delineate two time periods (1998-2002, 2008-2012) discussed later.

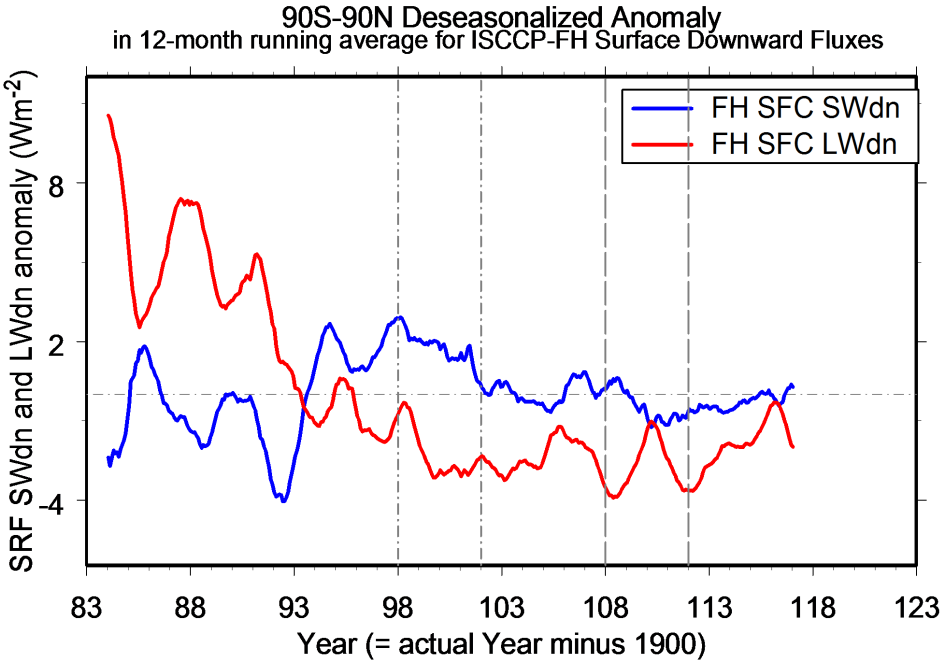
90S-90N Deseasonalized Anomaly
in 12-month running average for ISCCP-FH Surface Downward Fluxes
FH SFC SWdn
FH SFC LWdn
SRF SWdn and LWdn anomaly (Wm-2)
8
2
-4
83
88
93
98
103
108
113
118
123
Year (= actual Year minus 1900)

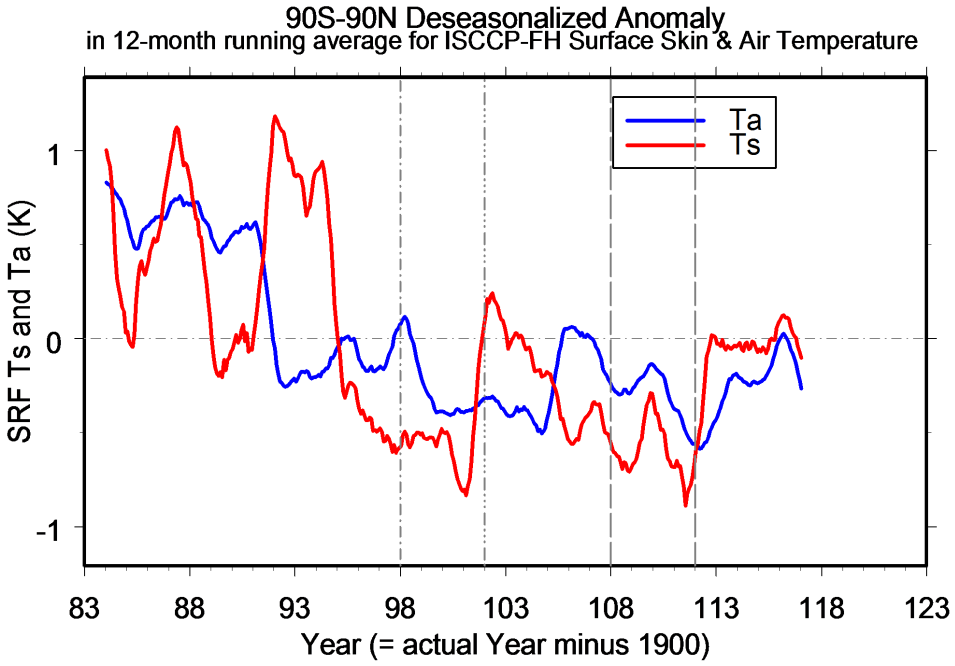
90S-90N Deseasonalized Anomaly
in 12-month running average for ISCCP-FH Surface Skin & Air Temperature
Ta
Ts
SRF Ts and Ta (K)
1
0
-1
83
88
93
98
103
108
113
118
123
Year (= actual Year minus 1900)

Figure 3. (Upper panel) Deseasonalized anomalies (shown as 12-month running averages) of global monthly mean downwelling SRF fluxes (Wm^{-2}) from FH for SWdn (blue curve) and LWdn (red curve). (Lower panel) Deseasonalized anomalies (shown as 12-month running averages) of global monthly mean near-surface air temperature (TA, blue curve) and surface skin temperature (TS, red curve) in Kelvins from ISCCP-FH. The vertical lines delineate two time periods (1998-2002, 2008-2012) discussed later.

There could also be subtle differences in the treatment of angle dependencies of the direct measurements, which have to be corrected, and the radiative transfer calculations. The satellite radiance measurements are converted to fluxes using empirical angle dependence models that have different but much more detailed scene dependencies for CERES than for ERBE (Loeb et al., 2001; Su et al., 2015a,b). The surface measurements have to be corrected for sensor angle dependence (e.g., Michalsky et al., 1999).

The satellite-based flux data products represent larger areas (of order 100 km in size) than the surface measurements (of order 50 km in size), which introduce differences in the presence of incomplete cloud cover. The radiative transfer calculations ignore small lateral exchanges (a better approximation at larger scales). Zhang et al. (2010) show that simple comparisons of the satellite-based products with surface measurements exhibit significantly larger differences if cloud and atmospheric conditions are not matched: rms differences in SW fluxes decrease by a factor of about two if cloud cover and optical thickness agree and LW flux rms differences decrease by as much as 30% if cloud cover and atmospheric temperature are matched with biases almost eliminated.

Another systematic difference is that ERBE/CERES define the top-of-atmosphere to be at 30 km and 20 km, respectively (Barkstrom et al., 1989 for ERBE, Loeb et al., 2018 for CERES), whereas FC/FD/FH define top-of-atmosphere at 100km. In FH the average differences in upward fluxes between the 100 hPa level and TOA imply that the flux difference related to this difference in reference level is < 1 Wm^{-2} for SW but could be as much as 2-3 Wm^{-2} for LW, which might be part of the lower FH values relative to ERBE/CERES (Table 2).

In summary, the comparison of FH with other direct measurements supports the uncertainty estimates shown in Tables 1 and 2.

Despite the magnitude of the estimated uncertainties of the monthly mean FH fluxes (Table 1), the long-term record of global mean net flux anomalies at TOA over about the last 15 years shows fair agreement with the CERES (SYN1deg Ed4.1) record, especially in SWnet (Fig. 2) (cf. EBAF Ed4.1 anomalies in Loeb et al., 2021). This comparison provides an additional evaluation of FH. The longer FH record suggests that the recent increase in SWnet (decreased albedo, see also Goode et al. 2021) may not be a trend but a long-term variation. However, the magnitude of the recent changes in LWnet in FH (decreased emission from about 2005 to 2012 and increased emission to 2017) is more than

twice as large as shown in the CERES record. The larger variability in the FH record in the 1980s and 1990s, exclusive of that associated with Pinatubo in 1991-1993, may be related to more variability in the ISCCP satellite coverage; however Zhang et al. (2004) show that the monthly average SWup and LWup flux anomalies in the tropics for FD for 1985-1999 agree with those from the ERBS record (Wielicki et al., 2002; Wong et al., 2006) to within about 1 Wm^{-2} (correlation about 0.8).

At the surface the global mean downwelling flux anomalies from FH are shown in Fig. 3 (upper panel). As discussed in Rossow and Zhang (1995) and Zhang et al. (2010), such comparisons (with surface station observations) are affected by the point-to-area mismatch of atmospheric conditions, so we focus on only the larger scale tendencies. Several analyses of surface measurements of SWdn − spatial coverage limited to land stations − have suggested an overall decrease from about 1960 to about 1990 and an increase afterwards into the early 2000s (Wild et al., 2005, cf. Wild, 2009). An increase after 2000 (to around 2008 and then a second increase after a short decrease) is consistent with the recent changes from CERES (Fig. 2). The FH record for SWdn is qualitatively similar if trend lines are fit to the periods before Pinatubo and after 2000, but shows that the peak in the late 1990s is larger than the values after 2005. Pinker et al. (2005) show other similar results based on the ISCCP-D data with an increase from 1983 to about 2001.

The LWdn in FH shows a very large anomaly declining rapidly at the beginning of the record until the late 1990s. After that there is an increase by a little less than 2 Wm^{-2}. Stephens et al. (2012) calculate an increasing LWdn under clear conditions over ocean by 3 Wm^{-2} from 1988-2008, based on SST, column water vapor and CO2 abundance determinations. The FH calculations (and previous versions) account for increasing CO2 and CH4 abundances, which should produce an increase in LWdn, all other things being equal; but as Fig 3 (lower panel) shows, the near-surface air temperature (Ta) and skin temperatures (Ts) from ISCCP-H used in FH are generally decreasing. The magnitude of the decrease is only about 1 K, but surface-based temperature records suggest an increase a little less than 1K over this same period (GISTEMP Team, 2021). The air temperatures (and humilities not shown) in ISCCP-H and FH show a small downward trend and small (1 K) discontinuities that are related to changes in the NNHIRS temperature and humidity retrievals between satellites in the HIRS series; this behavior of the HIRS retrievals propagates into the FH LW results. The overall downward trend in FH LWdn at SRF is likely due to the properties of the atmospheric data used in the calculations, but the magnitude of the uncertainties, at least from the 1990s onward, is similar to the estimate shown in Table 1.

Overall, while these long-term results from FH might be taken to show good accuracy relative to direct measurements, especially for the SW fluxes, the disagreements shown in Figs. 2 and 3 are well within the estimated uncertainties.

5 Some features of the long-term FH record

Table 3 compares the flux results from all three versions as global mean values averaged over the same five year period (seasonal months for April 1985 − January 1989). The systematic decrease of SWup at TOA and SWdn at SRF as well as increase of SWnet in ATM from FC to FH reflects the addition of more atmospheric absorption mostly by gases, a little by aerosols, and by subtle changes of ice cloud scattering. An increase of surface albedo from 12.7 to 13.7% between FD and FH is related to the added treatment of aerosols in ISCCP-H and a more detailed climatology in FH. The small decrease in LWup (and increase in LWcre) at TOA between FD and FH is related to small increases of high-level cloudiness (in FC only the average cloud top temperature over each map grid domain is used whereas FD and FH determine fluxes for a distribution of cloud properties within each domain). Despite the elimination of extreme surface temperatures in ISCCP-H (Rossow et al., 2022), SRF LWup increased slightly in FH compared with FD. Small changes in the treatment of low cloud base estimates, as well as the changes in atmospheric temperature-humidity, caused a decrease of LWcre at SRF for FH. In general, however, the overall changes from FC to FH are relatively small, similar in magnitude to the estimated uncertainties.

Table 3. Comparison of some global-time-average flux results from 16 seasonal months for the same four year period (April 1985 to January 1989) from the three versions of calculations (all are in Wm^{-2} except albedo in %)†.

Quantity	FC	FD	FH
TOA			
SWdn	341.63	341.84	340.30
SWup	111.50	105.58	104.62
LWup	234.24	233.15	231.49
SWnet	230.13	236.26	235.69
LWnet	-234.24	-233.15	-231.49
NET	-4.11	3.10	4.20
SWcre	-53.72	-50.39	-48.95
LWcre	21.27	26.21	28.29
Albedo	32.6	30.9	30.7
Atmosphere			
SWnet	65.04	70.83	77.37
LWnet	-188.41	-182.03	-179.85
NET	-123.37	-111.20	-102.47
SWcre	-1.57	2.90	2.53
LWcre	-3.62	-3.08	7.08
Surface			
SWdn	193.40	189.42	183.43
SWup	28.31	24.00	25.11
LWdn	348.30	344.59	345.95
LWup	394.13	395.71	397.59
SWnet	165.09	165.42	158.31
LWnet	-45.84	-51.12	-51.64

Quantity	FC	FD	FH
NET	119.25	114.30	106.67
SWcre	-52.15	-53.29	-51.48
LWcre	24.89	29.30	21.21
Albedo	14.6	12.7	13.7

† Cloud Radiative Effect (CRE as used in SWcre and LWcre for SW and LW CRE, respectively) is for net fluxes, positive sign means radiative heating in the system (the earth-atmosphere, earth or atmosphere system for TOA, surface or atmosphere) as conventionally defined. The original FH's 110-km map is re-gridded to 280-km map, the same as FC's and FD's map, before averaging.

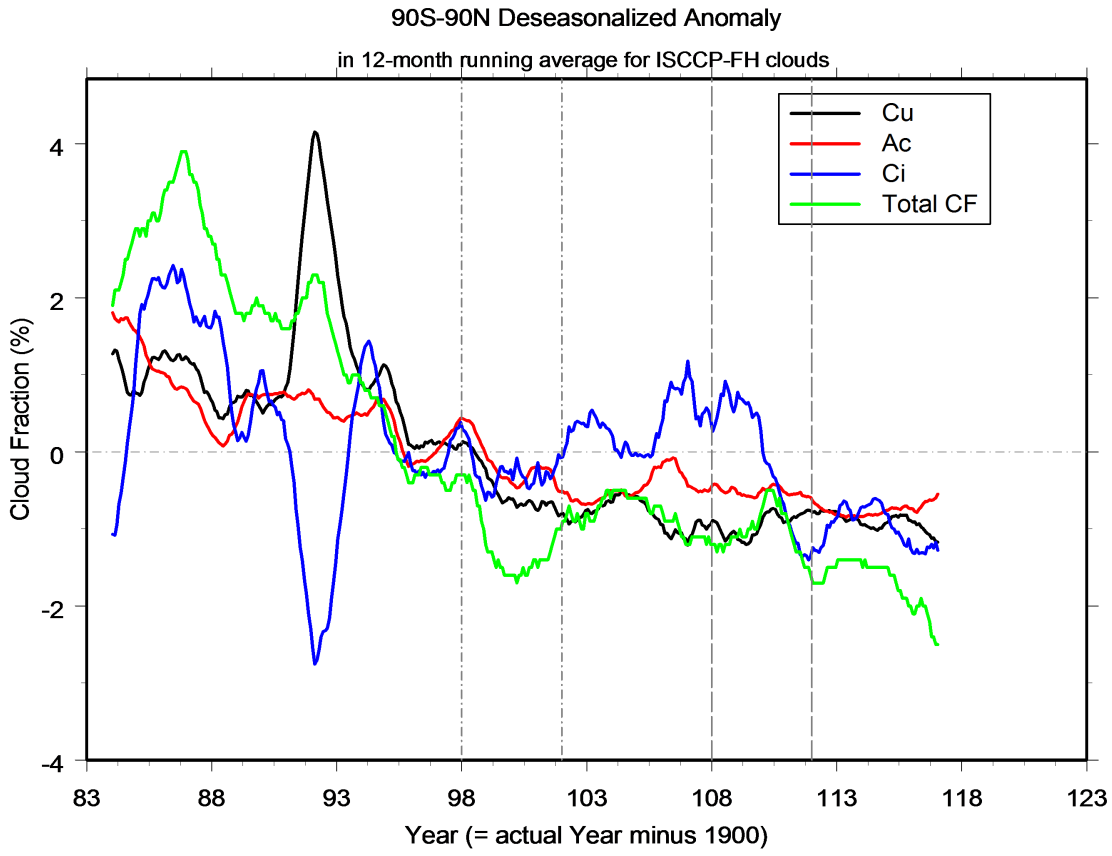

Figure 4. Deseasonalized anomalies (shown as 12-month running averages) of

global monthly mean total (green curve) cloud amount (%) and the amounts of cirrus (blue curve), altocumulus (red curve) and cumulus (black curve) as defined by in ISCCP-H but modified for FH: added cumulus to account for upper-level-cloud overlap and shifted altocumulus to cirrus to account for effect of cloud overlap on cirrus.

Ever since the late 1980s, the ISCCP cloud dataset has shown an overall decline of global mean cloud amount (CA), now also seen in other datasets (Karlsson and Devasthale 2018). The decrease in ISCCP CA is about 0.06 from 1986-2018, which may be exaggerated by 0.01-0.02 by artifacts in earlier years (Rossow et al., 2022). The large variations in the early 1990s are caused by partial detection as cloud of the thick stratospheric aerosol from the Mt. Pinatubo volcano. Looking at the variations of cloud types, defined in ISCCP by combinations of cloud top pressure-optical thickness (PC-TAU) and phase, shows that the global decrease appears solely in the optically thinnest types, mostly cumulus (Cu) and altocumulus (Ac) with some cirrus (Ci), as shown in Fig. 4. The results shown here are the version used in FH, where there have been adjustments of the ISCCP-H cloud type amounts that add some Cu amount and shift some middle-level clouds to cirrus to account for layer-overlap effects (cf. Rossow and Zhang 2010), increasing/decreasing the magnitude of the Ci/Ac changes. As there is no corresponding increase in the optically thicker cloud types (not shown), this change is not consistent with a drift of the VIS calibration (cf. Rossow and Ferrier, 2015), even though the overall average TAU does increase because of the decreased amount of thinner clouds included in the average. Moreover, if a drift of VIS calibration were the cause, the changes in these three cloud types would be strongly correlated, but only the changes in Cu and Ac are correlated (coefficient r = 0.8), not Ci (r < 0.4 with Ac but r = 0 with Cu). The key is that total CA in the ISCCP data is insensitive to calibration changes (see Fig. 2.2 in Appendix 2 in Stubenrauch et al. 2012) because the cloud detection each month is made relative to that month's determination of clear radiances: the global mean surface reflectance shows no trend. There is also supporting evidence from CERES, as shown in Fig. 2, indicating a decline in the global mean albedo since the early 2000s (Loeb et al., 2021), and from an observed corresponding increase in surface solar insolation in the 1990s (Wild et al., 2005; Pinker et al., 2005).

Although the simultaneous variations of many cloud, atmosphere and surface properties effect the flux anomalies (Fig. 2, 3), the leading single-variable anomaly correlations are as follows (all other correlation values are much smaller). At TOA, the leading correlation with variations of SWnet is changes of Cu amount (r = −0.5), which are, in turn, correlated with TS variations (r = 0.7, but this connection might be distorted by the fact that the TS values come from satellite infrared measurements, which are clear-sky biased). The variations of SWcre are dominated by overall changes in TAU (r = −0.8). The TOA LWnet variations are strongly correlated with changes in Ac amount (r = 0.7) and secondarily with changes in mid-troposphere water vapor (r = 0.5); however, the changes in TOA LWcre are dominated by changes in

Ci amount (r = 0.8) and near-surface air temperature, TA (r = 0.7), but not the mid-troposphere temperature (T500 r < 0.2). Correlations of SRF SWnet are similar to those at TOA, but the SRF LWnet and LWcre are more correlated with temperature and humidity changes than with cloud changes (although Ci amount variations explain some of the LWcre variance). The ATM SWnet is much more strongly affected by atmospheric humidity changes (precipitable water at mid-troposphere, PW500 r = 0.8), but the SWcre changes are dominated by changes in Ci amount (r = −0.8). Likewise the ATM LWnet and LWcre are affected most by changes in atmospheric temperature (r = −0.5, 0.7 respectively, with TA), although Ci amount is equally important to LWcre variations (r = 0.8).

6 Discussion of some possible feedbacks implied in an example of transient change

The period from the late 1990s to the early 2010s is notable for a number of reasons: (1) it was framed at the beginning by a very strong El Nino in 1997-1998 and La Nina from 1999-2001 and at the end by a strong La Nina in 2010-2012 with some weaker events in between (www.cpc.ncep.noaa.gov/data/indices/oni.ascii.txt), (2) the PDO index tracked the ENSO index in these framing events from strongly positive switching to negative at the beginning to persistently negative at the end, but weakly positive in between (www.ncei.noaa.gov/pub/data/cmb/ersst/v5/index/ersst.v5.pdo.dat), and (3) there was a significant slowing of the rate of increase of global annual mean surface temperature as compared to the decades before and after this period (www.data.giss.nasa.gov/gistemp). Figure 2 shows that the period from 1998 to 2012 was characterized in the FH data by a steady decrease of TOA SWnet (less heating) by a little more than 1.5 Wm^{-2} and an increase of TOA LWnet (less cooling) by a little more than 0.5 Wm^{-2}, giving an overall decrease TOA net flux by a little less than 1 Wm^{-2} (all quoted values are based on averages over 1998-2002 and 2008-2012 to

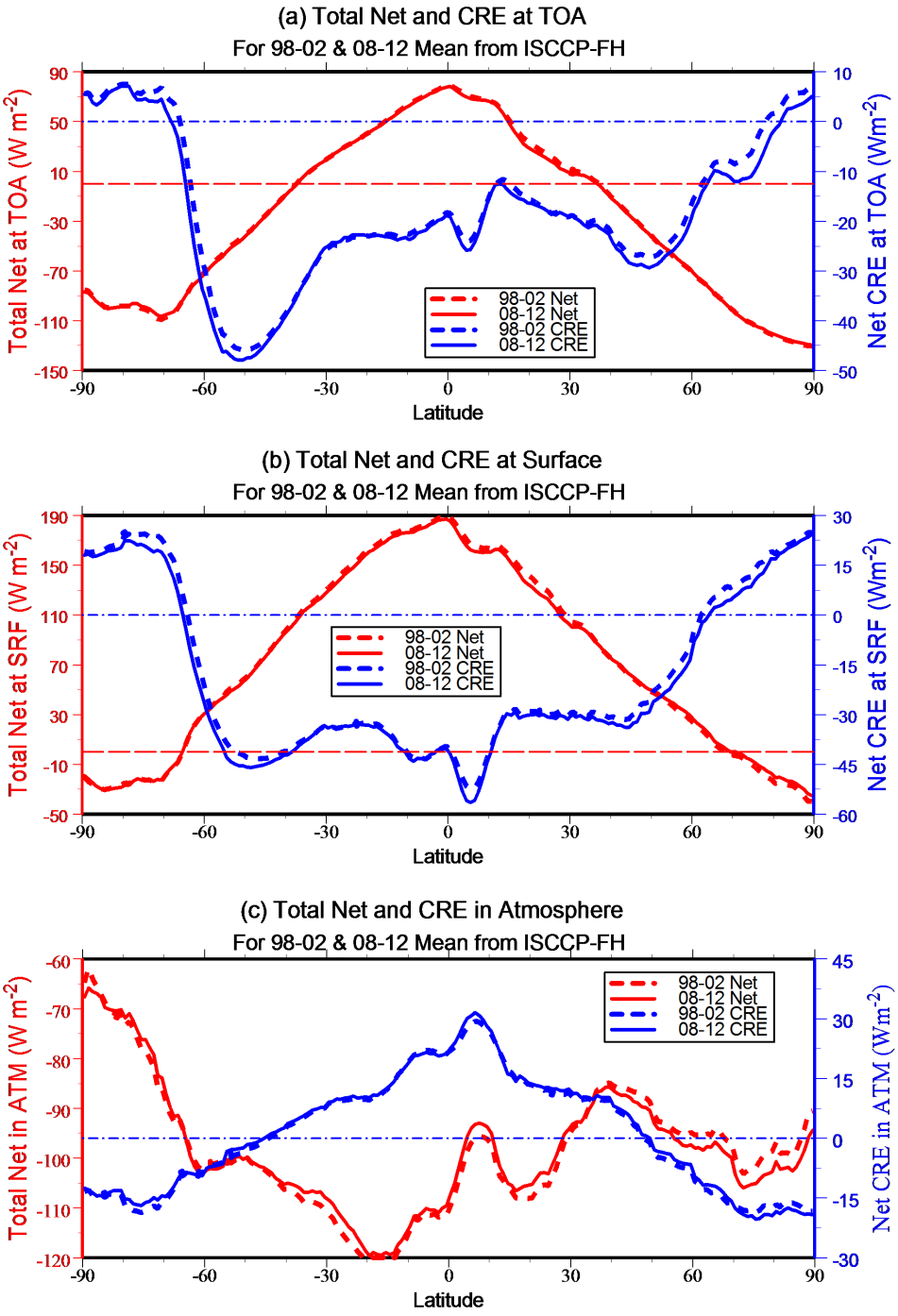
(a) Total Net and CRE at TOA
For 98-02 & 08-12 Mean from ISCCP-FH
Total Net at TOA (W m-2)
Net CRE at TOA (Wm-2)
Latitude
98-02 Net
08-12 Net
98-02 CRE
08-12 CRE
(b) Total Net and CRE at Surface
For 98-02 & 08-12 Mean from ISCCP-FH
Total Net at SRF (W m-2)
Net CRE at SRF (Wm-2)
Latitude
98-02 Net
08-12 Net
98-02 CRE
08-12 CRE
(c) Total Net and CRE in Atmosphere
For 98-02 & 08-12 Mean from ISCCP-FH
Total Net in ATM (W m-2)
Net CRE in ATM (Wm-2)
Latitude
98-02 Net
08-12 Net
98-02 CRE
08-12 CRE

Figure 5. Zonal mean Total Net Flux (red curves) and Cloud Radiative Effect (CRE, blue curves) in Wm^{-2} versus latitude averaged over two 5-yr periods (dashed curves 1998-2002, solid curves 2008-2012): (a) at TOA, (b) at surface and (c) in atmosphere. These two periods correspond, respectively, with positive and negative anomalies in TOA SWnet and negative and positive anomalies in TOA LWnet (Fig. 2).

represent the trends). Figure 3 shows a very similar anomaly of SRF SWnet with no significant change of SRF LWnet. Figure 4 shows a general increase of cirrus cloud amount by almost 2% over this period (with much smaller decrease of cumulus).

Figure 5a shows the zonal mean distribution of total net radiation and cloud radiative effect (CRE) at TOA averaged over the two time periods (1998-2002, 2008-2012) that correspond (Fig. 2), respectively, to the positive and negative anomalies of TOA SWnet and the negative and positive anomalies of TOA LWnet. The familiar total net flux distribution at TOA shows a net heating (SWnet > LWnet) in low to middle latitudes and a net cooling (SWnet < LWnet) at higher latitudes (cf. Zhang and Rossow, 1997; see also Kato et al., 2008). The net effect of clouds is to decrease lower latitude heating and increase higher latitude cooling (both negative CRE), except right at the poles where CRE is positive (cf. Zhang et al., 2004). The small SW and LW changes between these two periods are accounted for by cloud changes; although other atmospheric and surface properties play a role in the LW changes as discussed generally above (cf. Loeb et al. 2021), they are specifically related to the increase of cirrus in this particular period.

Table 4. Mean Net Fluxes and Cloud Radiative Effects at TOA, at Surface and in Atmosphere for 1998 to 2002 and 2008 to 2012 periods in Wm^{-2}.

	SWnet	LWnet	Net	SW_cre	LW_cre	Net_cre
	TOA					
1998-2002 mean	237.11	-232.78	4.33	-48.03	26.29	-21.74
2008-2012 mean	235.51	-231.97	3.54	-49.75	26.81	-22.93
	Surface					
1998-2002 mean	160.33	-53.37	106.97	-50.63	21.59	-29.04
2008-2012 mean	158.83	-53.50	105.33	-52.39	21.61	-30.79
	Atmosphere					
1998-2002 mean	76.78	-179.42	-102.64	2.61	4.70	7.30
2008-2012 mean	76.68	-178.47	-101.79	2.65	5.21	7.85

The global near-balance of TOA radiation splits into predominately SW heating of the surface and LW cooling of the atmosphere with clouds effects decreasing both (Table 3) as shown in Fig. 5b and 5c (cf. Zhang et al., 2004). The surface radiative heating (Fig. 5b) decreases with latitude becoming net cooling in the annual mean only in the polar regions because of lack of solar heating

in winter. The cloud effects at SRF decrease this heating at most latitudes (negative CRE) but cause surface heating at the poles (positive CRE). In other words clouds act to reduce the meridional gradient of surface heating that forces (in part) the oceanic circulation (cf. Zhang and Rossow, 1997; Kato et al., 2008). The net atmospheric cooling (Fig. 5c) is much larger at low to middle latitudes than in the polar regions (the polar cooling is much stronger in the north than in the south). Clouds reduce the ATM cooling at low to middle latitudes (positive CRE) and enhance it in the polar regions (negative CRE). In other words clouds act to reduce the meridional gradient of atmospheric cooling, effectively enhancing the

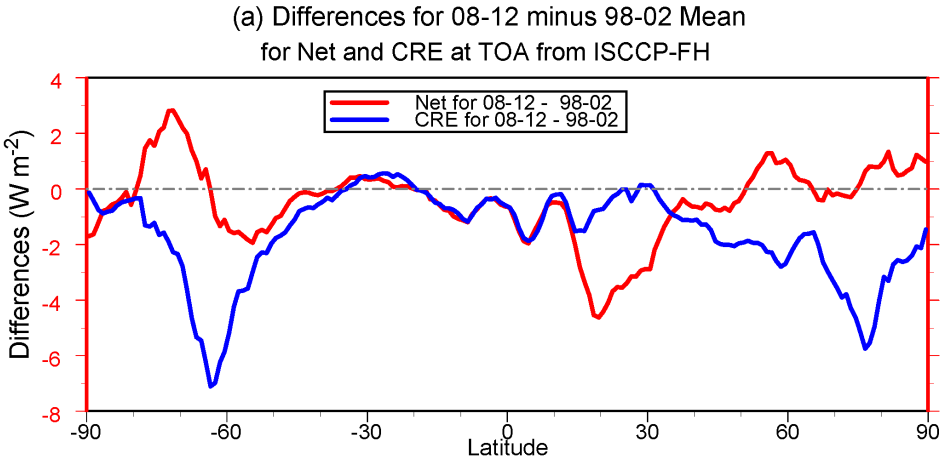
(a) Differences for 08-12 minus 98-02 Mean
for Net and CRE at TOA from ISCCP-FH
Net for 08-12 - 98-02
CRE for 08-12 - 98-02
Differences (W m-2)
4
2
0
-2
-4
-6
-8
-90
-60
-30
0
30
60
90
Latitude

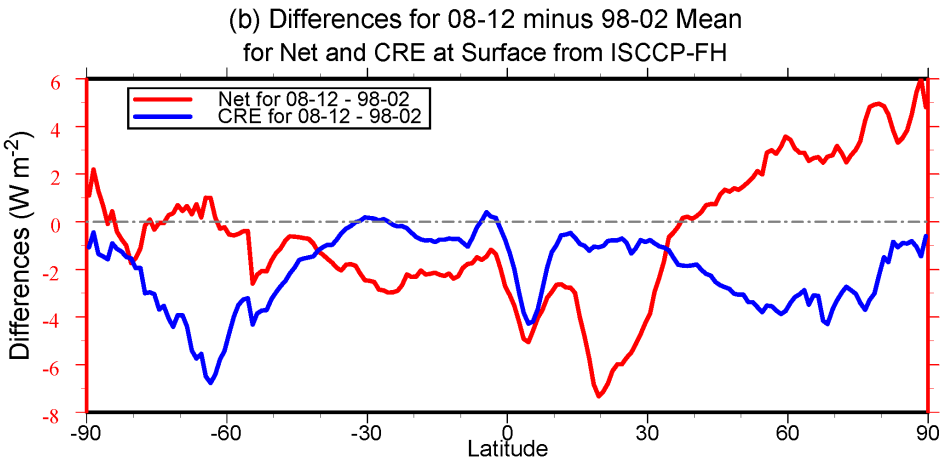
(b) Differences for 08-12 minus 98-02 Mean
for Net and CRE at Surface from ISCCP-FH
Net for 08-12 - 98-02
CRE for 08-12 - 98-02
Differences (W m-2)
6
4
2
0
-2
-4
-6
-8
-90
-60
-30
0
30
60
90
Latitude

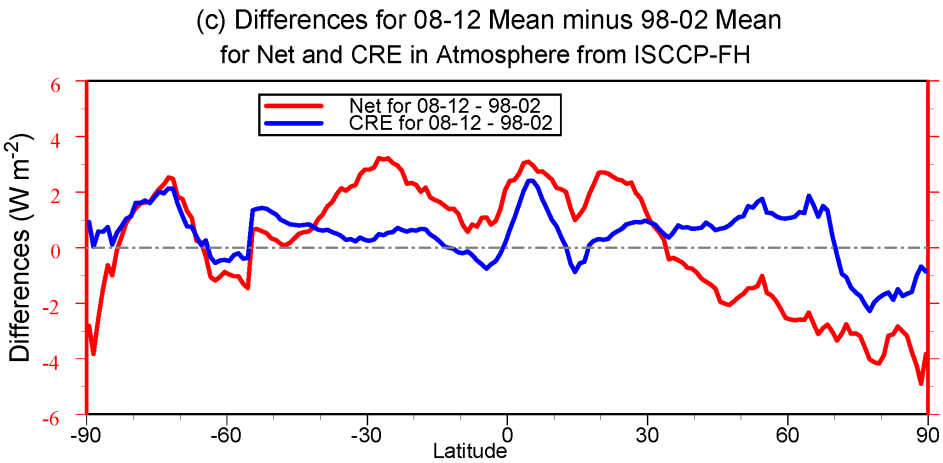
(c) Differences for 08-12 Mean minus 98-02 Mean
for Net and CRE in Atmosphere from ISCCP-FH
Net for 08-12 - 98-02
CRE for 08-12 - 98-02
Differences (W m-2)
6
4
2
0
-2
-4
-6
-90
-60
-30
0
30
60
90
Latitude

Figure 6. Differences between two 5-yr periods (2008-2012 minus 1998-2002) of the zonal mean Total Net Flux (red curve) and ATM CRE (blue curve) in Wm^{-2} versus latitude: (a) at TOA, (b) at surface and (c) in atmosphere.

heating gradient that forces the atmospheric circulation (cf. Zhang and Rossow, 1997; Kato et al., 2008).

All of the decrease of TOA SWnet (less heating) between 1998 and 2012 occurred at SRF and all of the increase of TOA LWnet (less cooling) occurred in the atmosphere (Table 4). The corresponding very small changes in the latitudinal distribution of net fluxes and CRE in Fig, 5 are better shown in Fig. 6 as the differences, 2008-2012 average minus 1998-2002 average, representing the trend from 1998 to 2012. The global average decrease of TOA total net flux over this period appears as a decrease at low to middle latitudes, but there is also an increase (reduced cooling) in the polar regions (Fig. 6a). The global mean decrease of total net flux at TOA is caused almost entirely by cloud effects on the SW offset by a weak effects on LW: Fig. 6a shows that the CRE is (mostly) negative at all latitudes but much more so at higher latitudes. However the changes in TOA total net flux confuse changes in SW forcing at the surface with changes in the LW response of the atmosphere, so separating the TOA changes into their SRF and ATM components better reveals what happened between 1998 and 2012. To keep the signs straight in what follows, the surface net flux changes are described as increases/decreases of heating and the atmospheric net flux changes are described as increases/decreases of cooling.

The net flux changes at SRF from 1998-2002 to 2012-2016 (Fig. 6b) show a very different pattern in the two hemispheres. The heating in the tropics decreased (negative difference), more strongly in the north than the south; the cooling at the poles also decreased (positive difference), again more strongly in the north than the south. These differences represent a decrease in the equator-to-pole heating gradient over this period. At middle latitudes the surface heating decreased in the southern hemisphere and increased in the northern hemisphere, but this pattern seems consistent with the overall change of the PDO index from positive to negative over this period, which would be a negative change of SST in the tropical Pacific and positive change of SST in the north Pacific. The overall pattern of change implies a weaker meridional gradient in radiative heating for the oceanic circulation, consistent with the cooling (warming) of SST in the tropics (midlatitudes). These net flux changes are mediated by the cloud changes: negative SRF CRE at lower latitudes shows only a very small decrease (becoming more negative) in the tropics and subtropics, but more substantial decreases at higher midlatitudes, related to a very small decrease of cumulus and altocumulus clouds (Fig. 4). Near the poles, where the SRF Net switches from negative to positive, it also decreases (becoming less positive). If the cloud-induced radiative flux changes from 1998 to 2012 − a reduction of the cloud decrease the meridional heating gradient − are indirectly related (through ocean-atmosphere interaction) to a change of the ocean circulation associated with the

reduced meridional temperature gradient (positive to negative PDO index), then they imply a positive cloud-radiative feedback on these ocean changes.

From 1998-2002 to 2008-2012, the ATM cooling decreased at lower latitudes (positive difference, a heating) and increased at higher latitudes (negative difference, a cooling), especially in the northern hemisphere (Fig. 6c). This implies an enhancement of the meridional radiative cooling gradient forcing the atmospheric circulation. The positive ATM CRE at low latitudes slightly increased (more heating related to increased cirrus) and the negative ATM CRE in the polar regions behaved differently in the north and south, decreasing in the north (decreased cooling effect) and increasing in the south (increased cooling effect). If these cloud-radiative changes are caused by a weakening of the atmospheric circulation, as might be expected from the decrease of the SST meridional gradient with the PDO phase change (see Chen et al. 2002 that find a strengthening circulation for an opposite trend in the 1990s), then the changes imply a negative feedback on the atmospheric circulation.

The opposite sense of these (possible) transient cloud-radiative feedbacks on the coupled atmospheric and oceanic circulations on a decadal time scale may come about because of the separate SW heating of SRF and LW cooling of ATM and because of the different SW and LW CRE by different cloud types. A similar opposite effect is seen in the partitioning of average cloud-radiative effects on the mean circulations discussed in Zhang and Rossow (1997) and Kato et al. (2008).

7 Conclusions

The FH radiative flux profile products provide global coverage at 100 km intervals and currently span the time period from July 1983 through June 2017 at 3 hr intervals. Comparisons with other more direct measurements suggest that the accuracy of these fluxes can provide useful diagnostic information about weather to interannual scale variations of radiation induced by changes in cloudiness as well as atmospheric and surface properties. Together with the variety of other satellite measurements, especially multi-spectral imagers, infrared spectrometers, microwave temperature-humidity sounders and active cloud and precipitation profilers, these results can be combined with global reanalyses of atmospheric motions to diagnose energy and water exchanges in the whole range of weather systems, e.g., analyses such as Jakob and Schumacher (2008), Haynes et al. (2011), Oreopolus et al. (2011), Booth et al. (2013), Polly and Rossow (2016), Masunaga and Luo (2016), Rossow et al. (2016), and those associated with slower "climate" variations such as MJO, seasons, and ENSO events, e.g., analyses such as Zhang and Rossow (1997), Kato et al. (2008), Tromeur and Rossow (2010). The clouds and radiative flux effects in weather and climate models can be evaluated, e.g., Tselioudis et al. (2021).

Acknowledgments

We would like to give special thanks to Dr. Reto Reudy who helped separate the radiation code (RadE) from NASA GISS GCM ModelE that makes possible to

initiate the ISCCP-FH project. We also especially thank Dr. Andrew A. Lacis and Dr. Valdar Oinas who participated in the development of the radiation code for the ISCCP-FH projec that made possible the ISCCP-FH flux data production. The development of the ISCCP-FH production code was funded by NOAA Climate Data Record Project (Grant NA11NES4400002 for 2011–2014). Computer facilities are supplied by NOAA's National Centers for Environmental Information and NASA Goddard Institute for space Studies. We thank Dr. Stefan Kinne who has provided us with Aerocom, MACv1 and MACv2, aerosol datasets. We also thank Dr. Paul W. Stackhouse and Dr. Shashi K. Gupta who have provided us with TSI datasets. Finally we thank CERES and BSRN teams for providing us with their datasets for the evaluation of the ISCCP-FH products.

Open Research

ISCCP-FH flux profile data products and documents can be accessed and downloaded through login at https://isccp.giss.nasa.gov/projects/flux.html. CERES SYN1deg Ed4 data may be ordered from https://ceres.larc.nasa.gov/data/#syn1deg-level-3, and for data Quality Summary, see https://ceres.larc.nasa.gov/documents/DQ_summaries/CERES_SY (Registration is required). BSRN data can be obtained from https://bsrn.awi.de/other/publications/establishme and-development-of-the-bsrn/. (Registration is required).

References

Barkstrom, B., Harrison, E., Smith, G., Green, R., Kibler, J., Cess, R., & the ERBE Science Team (1989). Earth Radiation Budget Experiment (ERBE) archival and April 1985 results. Bull. Amer. Meteor. Soc., 70 (10), 1254-1262, doi:10.1175/1520-0477(1989)070<1254:erbeaa>2.0.co;2.

Booth, J.F., Naud, C.M., & Del Genio, A.D. (2013). Diagnosing warm frontal cloud formation in a GCM: A novel approach using conditional subsetting. J. Climate, 26, 5827-5845, doi:10.1175/jcli-d-12-00637.1.

CERES Science Team (2013). CERES_SYN1deg_Ed3A Data Quality Summary, at https://ceres.larc.nasa.gov/documents/DQ_summaries/CERES_SYN1deg_Ed3A_DQS.pdf.

Chen, J., Carlson, B.E., & Del Genio, A.D. (2002). Evidence for the strengthening of the tropical general circulation in 1990s. Science, 295, 838-841, doi:10.1126/science.1065835.

Chen, T., & Rossow, W.B. (2002). Determination of top-of-atmosphere longwave radiative fluxes: A comparison between two approaches using ScaRab data. J. Geophys. Res., 107, D8, (1-14), doi:10.1029/2001jd000914.

DeAngelis, A.M., Qu, X., Zelinka, M.D., & Hall, A. (2015). An observational radiative constraint on hydrologic cycle intensification, Nature, 528, 249-253,

doi:10.1038/nature15770.

Driemel, A., Augustine, J., Behrens, K., Colle, S., Cox, C., Cuevas-Agulló, E., Denn, F., et al. (2018). Baseline Surface Radiation Network (BSRN): structure and data description (1992–2017), Earth Syst. Sci. Data, 10, 1491–1501, https://doi.org/10.5194/essd-10-1491-2018, 2018.

GISTEMP Team (2021). GISS Surface Temperature Analysis (GISTEMP), version 4. NASA Goddard Institute for Space Studies. Dataset accessed 20YY-MM-DD at https://data.giss.nasa.gov/gistemp/.

Goode, P.R., E. Palle, A. Shoumko, S. Shoumko, P. Montanes-Rodriguez and S.E. Koonin, 2021: Earth's albedo 1998-2017 as measured from earthshine. Geophys. Res. Lett., 48, (1-8), doi:10.1029/2021gl094888.

Goode, P.R., Palle, E., Shoumko, A., Shoumko, S., Montanes-Rodriguez, P., & Koonin, S.E. (2021). Earth's albedo 1998-2017 as measured from earthshine. Geophys. Res. Lett., 48, (1-8), doi:10.1029/2021gl094888.

Hansen, J., Fung, I., Lacis, A., Rind, D., Lebedeff, S., Ruedy, R., et al. (1988). Global climate changes as forecast by the Goddard Institute for Space Studies three-dimension model, J Geophys. Res., 93, 9341-9364, 1988.

Haynes, J.M., Jakob, C., Rossow, W.B. Tselioudis, G., & Brown, J. (2011). Major characteristics of southern ocean cloud regimes and their effects on the energy budget. J. Climate, 24, 5061-5080, doi:10.1175/2011jcli4052.1.

Jacob, C., & Schumacher, C. (2008). Precipitation and latent heating characteristics of the major tropical western Pacific cloud regimes. J. Climate, 21, 4348-4364. doi:10.1175/2008jcli2122.1.

Karlsson, K-G., & Devasthale, A. (2018). Inter-comparison and evaluation of the four longest satellite-derived cloud climate data records: CLARA-A2, ESA Cloud CCI V3, ISCCP-HGM and PATMOS-x. Remote Sensing, 2018, 10, 1567, (1-27), doi:10.3390/rs10101567.

Kato, S., Rose, F.G., Rutan, D.A., & Charlock, T.P. (2008). Cloud effects on the meridional atmospheric energy budget estimated from Clouds and the Earth's Radiant Energy (CERES) data. J. Climate, 21, 4223-4241, doi:10.1175/2008jcli1982.1.

Kelley, M., Schmidt, G.A., Nazarenko, L.S., Bauer, S.E., Ruedy, R., Russell, G. L., et al. (2020). GISS-E2.1: Configurations and climatology. Journal of Advances in Modeling Earth Systems, 12, e2019MS002025. Doi: 10.1029/2019MS002025.

Kinne, S., O'Donnel, D., Stier, P., Kloster, S., Zhang, K., Schmidt, H., et al. (2013). MAC-v1: A new aerosol climatology for climate studies. J. Adv. Modelling Earth Sys., 5, 704-740, doi:10.1002/jame.20035.2013.

Kinne, S. (2019). The MACv2 aerosol climatology. Tellus B: Chemical and Physical Meteorology, 71(1), 1–21. https://doi.org/10.1080/16000889.2019.1623639.

Kohsiek, W., Liebenthal, C., Foken, T., Vogt, R., Oncley, S.P., Bernhofer, Ch., & Debruin, H.A.R. (2006). The Energy Balance Experiment EBEX-2000. Part III: Behavior and quality of the radiation measurements. Boundary-Layer Meteor., (1-21), doi:10.1007/s10546-006-9135-8.

Lacis, A. A., & Oinas, V. (1991). A description of the correlated k distributed method for modeling nongray gaseous absorption, thermal emission, and multiple scattering in vertically inhomogeneous atmospheres. J. Geophys. Res., 96, 9027-9063, doi:10.1029/90jd01945.

Liu, Z., Kar, J., Zeng, S., Tackett, J., Vaughan, M., Avery, M., et al., (2019). Discriminating between clouds and aerosols in the CALIOP version 4.1 data products. Atmos. Meas. Tech., 12, 703-734, doi:10.5194/amt-12-703-2019.

Loeb, N.G., Priestley, K. J., Kratz, D. P., Geier, E. B., Green, R. N., Wielicki, B. A., et al. (2001). Determination of unfiltered radiances from the Clouds and the Earth's Radiant Energy System instrument. J. Appl. Meteor., 40, 822-835, doi:10.1175/1520-0450(2001)040<0822:dourft>2.0.co;2.

Loeb, N.G., Doelling, D.R., Wang, H., Su, W., Nguyen, C., Corbett, J. G., et al. (2018). Clouds and the Earth's Radiant Energy System (CERES) Energy Balanced and Filled (EBAF) top-of-atmosphere (TOA) Edition-4.0 data product. J. Climate, 31, 894-918, doi:10.1175/jcli-d-17-0208.1.

Loeb, N.G., Johnson, G.C., Thorsen, T.J., Lyman, J.M., Rose, F.G., & Kato, S. (2021). Satellite and ocean data reveal marked increase in Earth's heating rate. Geophys. Res. Lett., 48, (1-8), doi:10.1029/2021gl093047.

Mace, G.G., & Zhang, Q. (2014). The CloudSat radar-lidar geometric profile product (RL-GeoProf): Updates, improvements, and selected results. J. Geophys. Res. Atmos., 119, 9441-9462, doi:10.1002/2013jd021374.

Masunaga, H., & Luo, Z. J. (2016). Convective and large-scale mass flux profiles over tropical oceans determined from synergistic analysis of a suite of satellite observations. J. Geophys. Res. Atmos., 121, 7958-7974, doi:10.1002/2016jd024753.

Michalsky, H., Dutton, E., Rubes, M., Nelson, D. Stoffel, T., Wesley, M., et al., (1999). Optimal measurement of surface shortwave irradiance using current instrumentation. J. Atmos. Ocean Tech., 16, 55-69, doi:10.1175/1520-0426(1999)016<0055:omossi>2.0.c0;2.

Ohmura, A., Dutton, E.G., Forgan, B., Frohlich, C. Gilgen, H., Hegner, H., et al. (1998). Baseline Surface Radiation Network (BSRN/WCRP): New precision radiometry for climate research. Bull. Amer. Meteor. Soc., 79 (10), 2115-2136, doi:10.1175/1520-0477(1998)079<2115:bsrnbw>2.0.co;2.

Oreopoulos, L., & Rossow, W. B. (2011). The cloud radiative effect of ISCCP weather states. J. Geophys. Res., 116, (1-22), doi:10/1029/2010jd015472.

Oreopoulos, L., Mlawer, E., Delamere, J., Shippert, T., Cole, J., Fomin, B., et

al. (2012). The Continual Intercomparison of Radiation Codes: Results from Phase I. J. Geophys. Res., 117, D06118, (1-19), doi:10.1029/2011jd016821.

Philipona, R., Dutton, E.G., Stoffel, T., Michalsky, J., Reda, I., Stifter, A., et al. (2001). Atmospheric longwave radiance uncertainty: Pyrgeometers compared to an absolute sky-scanning radiometer, atmospheric emitted radiance interferometer, and radiative transfer model calculations. J. Geophys. Res., 106, D22, 28,129-28,141, doi:10.1029/200jd000196.

Pinker, R.T., Zhang, B., & Dutton, E.G. (2005). Do satellites detect trends in surface solar radiation? Science, 308, 850-854, doi:10.1126/science.1103159.

Polly, J., & Rossow, W.B. (2016). Distribution of midlatitude cyclone attributes based on the MCMS database. J. Climate, 6483-6507, doi:10.1175/jcli-d-15-0857.1.

Raschke, E., Kinne, S., Rossow, W.B., Stackhouse, P.W., & Wild, M. (2016). Comparison of radiative energy flows in observational datasets and climate modeling. J. Appl. Meteor. Climatol., 55, 93-117, doi:10.1175/jamc-d-14-0281.1.

Rossow, W.B., & Zhang, Y-C. (1995). Calculation of surface and top-of-atmosphere radiative fluxes from physical quantities based on ISCCP datasets, Part II: Validation and first results. J. Geophys. Res., 100, 1167-1197, doi:10.1029/94jd02746.

Rossow, W.B., Zhang, Y-C., & Wang, J-H. (2005). A statistical model of cloud vertical structure based on reconciling cloud layer amounts inferred from satellites and radiosonde humidity profiles. J. Climate, 18, 3587-3605, doi:10.1175/jcli3479.1.

Rossow, W.B., & Zhang, Y-C. (2010). Evaluation of a statistical model of cloud vertical structure using combined CloudSat and CALIPSO cloud layer profiles. J. Climate, 23, 6641-6653, doi:10.1175/2010jcli3734.1.

Rossow, W.B., & Ferrier, J. (2015). Evaluation of long-term calibrations of the AVHRR visible radiances. J. Atmos. Ocean Tech., 32, 744-766, doi:10.1175/jtech-d-14-00134.1.

Rossow, W.B., Zhang, Y-C., & Tselioudis, G. (2016). Atmospheric diabatic heating in different weather states and the general circulation. J. Climate, 29, 1059-1065, doi:10.1175/jcli-d-15-0760.1.

Rossow, W.B. (2017). ISCCP H-Version – Climate Algorithm Theoretical Basis Document, NOAA Climate Data Record Program (CDRP-ATDB-0.872) Rev 0 (2017), 301 pp., Available at

http://www1.ncdc.noaa.gov/pub/data/sds/cdr/CDRs/Cloud_Properties-ISCCP/AlgorithmDescription_01B-29.pdf

Rossow, W.B., Knapp, K.R., & Young, A.H. (2022). International Satellite Cloud Climatology Project: Extending the record. J. Climate, 35. 141-158, doi:10.1175/jcli-d-21-0157.1.

Rothman, L. S., & coauthors (2013). The HITRAN2012 molecular spectroscopic database, J. Quantitative Spectroscopy & Radiative Transfer, 130(2013), 4-50.

Stackhouse, P.W., Cox, S.J., Mikovitz, J.C., & Zhang, T. (2021). GEWEX (Global Energy and Water Exchanges Project) Surface Radiation Budget (SRB) Release 4 Integrated Product (IP4) Algorithm Theoretical Basis Document and Evaluation, https://asdc.larc.nasa.gov/documents/srb/SRB_Rel4-IP_ATBD.pdf.

Stephens, G.L., Wild, M., Stackhouse, P.W., L'Ecuyer, T., Kato, S., & Henderson, D.S. (2012). The global character of the flux of downward longwave radiation. J. Climate, 25, 2329-2340, doi:10.1175/jcli-d-11-00262.1.

Stubenrauch, C., Rossow, W.B., & Kinne, S. (2012). GEWEX Assessment of Global Cloud Data Sets from Satellites. WCRP 23/2012, November, pp. 176.

Su, W., Corbett, J., Eitzen, Z., & Liang, L. (2015a). Next-generation angular distribution models for top-of-atmosphere radiative flux calculations from CERES instruments: methodology. Atmos. Meas. Tech., 8, 611-632, doi:10.5194/amt-8-611-2015.

Su, W., Corbett, J., Eitzen, Z., & Liang, L. (2015b). Next-generation angular distribution models for top-of-atmosphere radiative flux calculations from CERES instruments: validation. Atmos. Meas. Tech., 8, 3297-3313, doi:10.5194/amt-8-3297-2015.

Tromeur, E., & Rossow, W. B. (2010). Interaction of tropical deep convection with the large-scale circulation in the Madden-Julian oscillation. J. Climate, 23, 1837-1853, doi:10.1175/202009jcli3240.1.

Tselioudis, G., Rossow, W.B., Jakob, C., Remillard, J., Tropf, D., & Zhang, Y-C. (2021). Evaluation of clouds, radiation, and precipitation in CMIP6 models using global Weather States derived from ISCCP-H cloud property data. J. Climate, 34, 7311-7324, doi:10.1175/jcli-d-21-0076.1.

Wielicki, B.A., Wong, T., Allan, R.P., Slingo, A., Kiehl, J.T., Soden, B.J., et al. (2002). Evidence for large decadal variability in the tropical mean radiative energy budget. Science, 295, 841-844, doi:10.1126/science.1065837.

Wild. M., Gilgen, H., Roesch, A., Ohmura, A., Long, C.N., Dutton, E.G., et al. (2005). From dimming to brightening: Decadal changes in solar radiation at Earth's surface. Science, 308, 847-850, doi:10.1126/science.1103215.

Wild, M. (2009). Global dimming and brightening: A review. J. Geophys. Res., 114, D00D16, (1-31), doi:10.1029/2008jd011470.

Wong, T., Wielicki, B.A., Lee, R.B., Smith, G.L., Bush, K.A., & Willis, J.K. (2006). Reexamination of the observed decadal variability of the Earth radiation budget using altitude-corrected ERBE/ERBS nonscanner WFOV data. J. Climate, 19, 4028-4040. doi:10.1175/jcli3838.1.

Young, A.H., Knapp, K.R., Inamdar, A., Hankins, W., & Rossow, W.B. (2018). The International Satellite Cloud Climatology Project H-Series Climate Data Record Product. Earth System Science Data, 10, 583-593, doi:10.5194/essd-10-583-2018.

Zhang, Y-C., Rossow, W.B., & Lacis, A.A. (1995). Calculation of surface and top of atmosphere radiative fluxes from physical quantities based on ISCCP datasets 1. Method and sensitivity to input data uncertainties. J. Geophys. Res., 100, 1149-1165, doi:10.1029/94jd02747.

Zhang, Y-C., & Rossow, W.B. (1997). Estimating meridional energy transports by the atmospheric and oceanic general circulations using boundary fluxes. J. Climate, 10, 2358-2373, doi:10.1175/1520-0442(1997)010<2358:emetbt>2.0.co;2.

Zhang, Y-C., Rossow, W.B., Lacis, A.A. Oinas, V., & Mishchenko, M. I. (2004). Calculation of radiative fluxes from the surface to top of atmosphere based on ISCCP and other global data sets: Refinements of the radiative transfer model and the input data. J. Geophys. Res., 109, D19105, (1-27), doi:10.1029/2003jd004457.

Zhang, Y., Rossow, W.B., & Stackhouse, P.W. (2006). Comparison of different global information sources used in surface radiative flux calculation: Radiative properties of the near-surface atmosphere. J. Geophys. Res., 111, D13106, (1-13), doi:10.1029/2005jd006873.

Zhang, Y-C., Rossow, W.B., & Stackhouse, P.W. (2007). Comparison of different global information sources used in surface radiative flux calculation: Radiative properties of the surface. J. Geophys. Res., 112, D01102, (1-20), doi:10.1029/2005jd007008.

Zhang, Y-C., Rossow, W.B., Long, C.N., & Dutton, E.G. (2010). Exploiting diurnal variations to evaluate the ISCCP-FD flux calculations and Radiative-Flux-Analysis-Processed Surface Observations from BSRN, ARM and SURFRAD. J. Geophys. Res., 115, D15105, (1-21), doi:10.1029/2009jd012743.

Zhang, Y-C. (2017). ISCCP-FH Radiative Flux Profile Produc, Climate Algorithm Theoretical Basis Document (C-ATBD), NOAA NCEI Climate Data Record (CDR) Program, 2017, https://isccp.giss.nasa.gov/pub/flux-fh/docs/C-ATBD_ISCCP-FH.pdf, through login to https://isccp.giss.nasa.gov/projects/flux.html.

Table 1. Comparison of 2007 monthly mean ISCCP-FH and FD TOA fluxes with CERES (Edition 3A, CERES Science Team, 2013) and SRF fluxes with BSRN (Ohmura et al., 1998) in Wm^{-2}. The uncertainty range is based on the normal deviations (rms distance of each point from the least squares linear fit) (Rossow and Zhang, 1995).

TOA		
	FH vs CERES	FD vs CERES
SWnet	-7 ± 6	-8 ± 6
Correlation for SWnet	0.99	0.99
LWnet	+7 ± 3	+3 ± 3
Correlation for LWnet	0.99	0.99
Overall uncertainty	10 Wm^{-2}	10 Wm^{-2}
Surface		
	FH vs BSRN	FD vs BSRN
SWnet	-1 ± 15	-4 ± 17
Correlation for SWnet	0.99	0.99
LWnet	-7 ± 12	+10 ± 14
Correlation for LWnet	0.97	0.97
Overall uncertainty	20 Wm^{-2}	20 W/m^{-2}

Table 2. Evolution of flux biases (Wm^{-2}) from comparisons with spatially matched ERBE or CERES at top-of-atmosphere and GEBA (Wild et al. 2017) or BSRN at surface (Driemel et al. 2018)†.

TOA			
	FC – ERBE	FD – ERBE	FH – CERES
SWup	+10.7	+4.7	+7.2 (+7.5, +5.0)
LWup	−1.1	−2.2	−7.1 (−7.0, −8.0)
Net	−9.3	−2.0	0.0 (−0.5, −3.2)
Surface			
	FC – GEBA	FD – BSRN	FH – BSRN
SWdn	+15.2	+2.0	−1.4
LWdn	−19.4	+2.2	−7.5
Net	N/A	N/A	(+4.1)

†The FC comparisons are based on 16 seasonal months over 1985 – 1989 as reported in Rossow et al. (1995). The FD comparison with ERBE is also based on the same 16 seasonal months as FC but the FD comparison with BSRN is based on all months over 1992 – 2001 as reported in Zhang et al. (2004). The FH comparisons are based on monthly means in 2007 from CERES (SYN1deg Ed3a) and BSRN; values in parentheses represent the bias with respect to CERES SYN1deg 4.1 for 2007–2009 period and EBAF 4.1 and 2001–2009 period, respectively, cited from Stackhouse et al. (2021).

Table 3. Comparison of some global-time-average flux results from 16 seasonal months for the same four year period (April 1985 to January 1989) from the three versions of calculations (all are in Wm^{-2} except albedo in %)†.

Quantity	FC	FD	FH
TOA			
SWdn	341.63	341.84	340.30
SWup	111.50	105.58	104.62
LWup	234.24	233.15	231.49
SWnet	230.13	236.26	235.69
LWnet	-234.24	-233.15	-231.49
NET	-4.11	3.10	4.20
SWcre	-53.72	-50.39	-48.95
LWcre	21.27	26.21	28.29
Albedo	32.6	30.9	30.7
Atmosphere			
SWnet	65.04	70.83	77.37
LWnet	-188.41	-182.03	-179.85
NET	-123.37	-111.20	-102.47
SWcre	-1.57	2.90	2.53
LWcre	-3.62	-3.08	7.08
Surface			
SWdn	193.40	189.42	183.43
SWup	28.31	24.00	25.11
LWdn	348.30	344.59	345.95
LWup	394.13	395.71	397.59
SWnet	165.09	165.42	158.31
LWnet	-45.84	-51.12	-51.64
NET	119.25	114.30	106.67
SWcre	-52.15	-53.29	-51.48
LWcre	24.89	29.30	21.21
Albedo	14.6	12.7	13.7

† Cloud Radiative Effect (CRE as used in SWcre and LWcre for SW and LW CRE, respectively) is for net fluxes, positive sign means radiative heating in the system (the earth-atmosphere, earth or atmosphere system for TOA, surface or atmosphere) as conventionally defined. The original FH's 110-km map is re-gridded to 280-km map, the same as FC's and FD's map, before averaging.

Table 4. Mean Net Fluxes and Cloud Radiative Effects at TOA, at Surface and in Atmosphere for 1998 to 2002 and 2008 to 2012 periods in Wm^{-2}.

	SWnet	LWnet	Net	SW_cre	LW_cre	Net_cre
	TOA					
1998-2002 mean	237.11	-232.78	4.33	-48.03	26.29	-21.74
2008-2012 mean	235.51	-231.97	3.54	-49.75	26.81	-22.93
	Surface					

	SWnet	LWnet	Net	SW_cre	LW_cre	Net_cre
1998-2002 mean	160.33	-53.37	106.97	-50.63	21.59	-29.04
2008-2012 mean	158.83	-53.50	105.33	-52.39	21.61	-30.79
	Atmosphere					
1998-2002 mean	76.78	-179.42	-102.64	2.61	4.70	7.30
2008-2012 mean	76.68	-178.47	-101.79	2.65	5.21	7.85